Australian Earthquake Engineering Society
2023 National Conference, 23-25 November 2023
Brisbane, Queensland, Australia

Identifying hidden faults using Coulomb stress change inversion: application to the 5.5 (mb) 1973 Picton Earthquake

Eric C Wang[1], Patrice F Rey[1] and Vasileios Chatzaras[1]

1. The University of Sydney, School of Geosciences, New South Wales, 2006, Australia

Abstract

Although Australia is perceived to be seismically stable, it experiences earthquakes that threaten major cities, as shown by the 1989 Newcastle earthquake (5.4 M_W), as well as the more recent 2021 Woods Point earthquake (5.9 M_W) and 2023 Sunbury earthquake (3.8 M_L) near Melbourne. Probabilistic seismic hazard modelling is an essential element in defining high-hazard areas and minimising risk. The mapping of active faults is an important component of seismic hazard modelling. However, their identification and characterisation are often challenging.

Following an earthquake, stress is redistributed in a way to load or unload surrounding faults, a process referred to as Coulomb stress change. The distribution of aftershocks, following a main earthquake, is the outcome of Coulomb stress change. Therefore, earthquake datasets can be analysed to infer the location of blind faults. The published focal mechanisms for the 1973 Picton earthquake suggest two possible fault sources. Here, we forward model Coulomb stress change associated with an earthquake to produce possible fault source and receiver models and predict aftershocks distribution. We show that this methodology can be utilised to document hidden faults quickly and efficiently, particularly in regions of low seismicity. We use the 1973 Picton earthquake (5.5 mb) and its associated cluster of aftershocks, which ruptured 90 km west-southwest of Sydney and 40 km southwest of Warragamba Dam. This earthquake is one of the largest recorded near Sydney, yet it has remained largely ignored.

Keywords: Coulomb stress change; fault identification; 1973 Picton Earthquake

1 Introduction

Earthquakes with magnitudes > 5 are not uncommon in Australia (Figure 1a). An issue of particular importance is that often earthquakes are not associated with known neotectonic faults. In densely populated regions with significant infrastructures, this impedes risk mitigation strategies. Prime examples include the 1989 Newcastle earthquake (5.4 M_W), the most devastating in Australian history, and the 1973 Picton earthquake (5.5 m_b), one of the largest magnitude earthquakes within the vicinity of Sydney. Both earthquakes show that cities such as Sydney, Newcastle, and Wollongong, the population of which has doubled over the past 50 years (Australian Bureau of Statistics, 2022), cannot ignore seismic risks. There is a need to better document the network of neotectonic faults on which cities are built. Here, we revisit the Picton earthquake's focal mechanisms and analyse aftershocks to identify hidden faults.

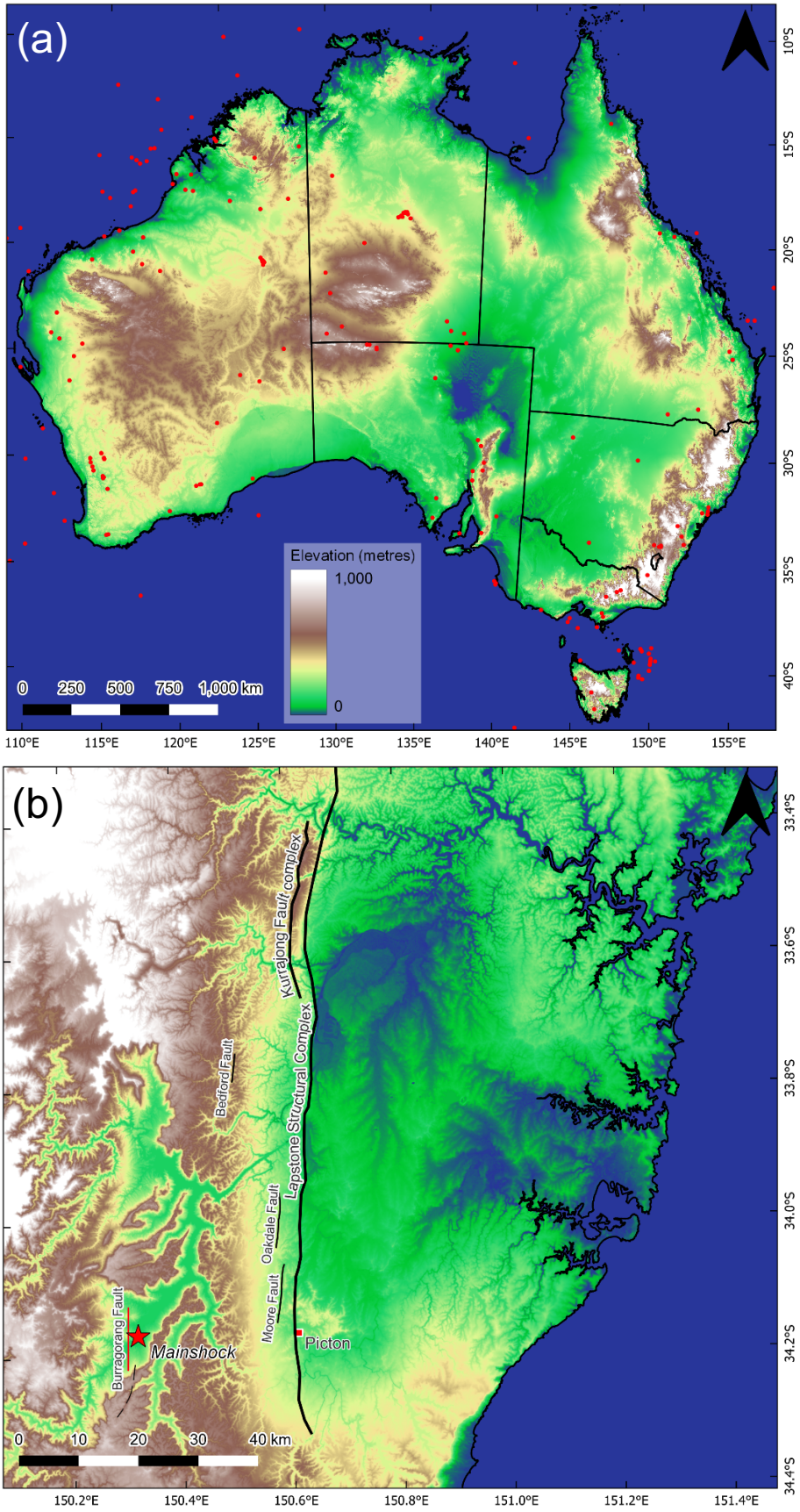

Figure 1. (a) Topographic map of Australia with all magnitude > 5 earthquakes since 1842 plotted as red points. (b) Topographic map of the Sydney Basin. Plotted are simplified depictions of the Lapstone Structural Complex and Kurrajong Fault Complex (from Allen (2021)), the 1973 Picton earthquake mainshock, various faults and a lineament (dashed line; from Colquhoun et al. (2022)), and the projected location of the Burragorang fault. Earthquake data is sourced from Geoscience Australia (2023); and digital elevation model is sourced from Gallant (2011).

The Blue Mountains is an uplifted region located west of metropolitan Sydney (Figure 1b) (Van der Beek et al., 2001; Fergusson et al., 2011; Fergusson & Hatherly, 2022). On its eastern margin is the Lapstone Structural Complex, a neotectonic feature that consists of a group of north-south striking high-angle faults (i.e., the Kurrajong Fault Complex), bounding the western side of an east-facing monocline (Lapstone Monocline) associated with moderately west-dipping faults (Figure 1b) (Branagan & Pedram, 1990; Fergusson et al., 2011; Fergusson & Hatherly, 2022).

In the early morning of March 10th 1973, an earthquake of magnitude (m_b) 5.5 struck 90 km southwest of Sydney CBD within the Southern Blue Mountains area, 20 km west of the Lapstone Structural Complex. The mainshock occurred at a depth of 21 km (Geoscience Australia, 2023), followed by a swarm of aftershocks in the coming months. The earthquake was felt throughout Sydney and as far as Canberra, with reports of the Sydney Harbour Bridge swaying. The strongest ground shakings were reported in the vicinity of Picton, Robertson, and Wollongong (Denham, 1976). Structural damage was concentrated on old masonry/brick buildings, largely in the form of minor to moderate cracks, brick dislodgement, and minor ground displacement (Dayer, 1976; Denham, 1976).

Initial focal mechanisms were dominantly reverse slip with a minor strike-slip component (Figure 2b and c) (Fitch, 1976; Mills & Fitch, 1977). An alternative focal mechanism by Leonard et al. (2002) shows a dominant strike-slip motion (Figure 2d). Analysis of aftershocks suggested a near vertical, north-south striking fault (hereafter Burragorang fault) (Mills & Fitch, 1977). In this paper, the aftershock locations and published focal mechanisms are used as a basis for source and receiver fault models for Coulomb stress change analysis. We also reprocess polarity station data to produce focal mechanisms that minimises polarity errors. These are compared to the Coulomb stress change analysis to identify acceptable fault source models.

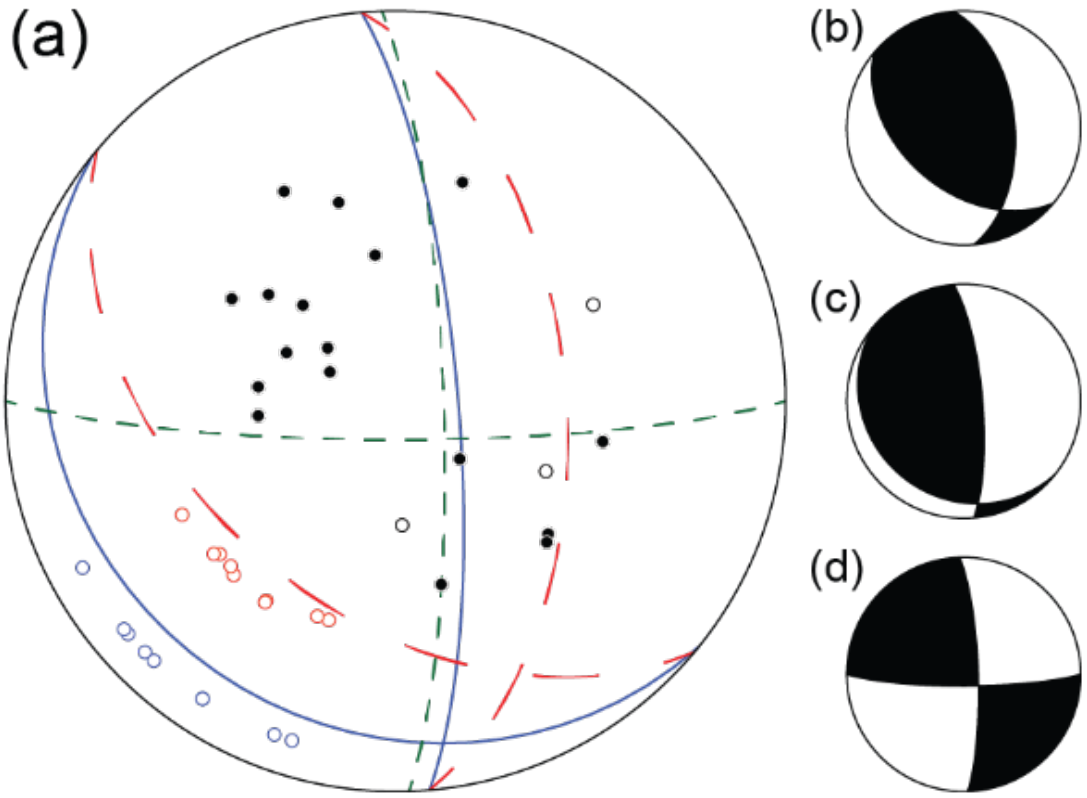

Figure 2. (a) Focal mechanism showing two station datasets from Fitch (1976) and Mills & Fitch (1977), or the original and updated station dataset, respectively. Both share the same polarities except for the southwest quadrant polarities, where the red circles are from Fitch (1976) and the blue circles from Mills & Fitch (1977). Compressional and dilatational polarities are represented by the solid and open circles, respectively. The red (long dashed), blue (solid line), and green (short dashed) nodal planes draw the focal mechanisms of (b) Fitch (1976); (c) Mills & Fitch (1977); and (d) Leonard et al. (2002), respectively.

2 Methods and Data

2.1 Coulomb Stress Change

Coulomb stress change, or Coulomb failure stress change (ΔCFS), describes the changes in local stress following a major earthquake (King et al., 1994). Positive ΔCFS brings faults closer to failure, resulting in increased seismicity/seismic potential, while negative ΔCFS reduces load and decreases seismic potential (Kilb et al., 2002). Studies have found a minimum earthquake stress change triggering threshold as low as 0.01 MPa (King et al., 1994), whilst others have suggested no threshold exists (Ziv & Rubin, 2000). Therefore, ΔCFS can be used to explain the spatial and/or temporal distribution of aftershocks, even for moderate sized earthquakes. ΔCFS is expressed as:

$$\Delta CFS = \Delta\tau + \mu'\Delta\sigma_n \quad (1)$$

Where $\Delta\tau$ is the shear stress change, μ' is the effective friction coefficient, and $\Delta\sigma_n$ is the normal stress change. The standard value of 0.4 is used as the effective friction coefficient. In our study, we use ΔCFS to infer the rupture source and slip direction. We utilise the Coulomb 3.4 software for ΔCFS analysis (Lin & Stein, 2004; Toda et al., 2005; Toda et al., 2011). The software allows the mapping of stress change induced by an earthquake on a source fault and on receiver fault/s (the fault/s that receives stress).

To calculate the amount of slip associated with the earthquake, conversion to moment magnitude (M_W) is required. Allen et al. (2018) provides recommendations for various magnitude conversions to M_W for Australian earthquakes. An average M_W of 5.4 was obtained from body wave magnitude (m_b), local magnitude (M_L), and surface-wave magnitude (M_S) conversion (see Table 1). Coulomb 3.4 estimates a net slip of 0.26 m for a M_W of 5.4.

Table 1. Conversion of the 1973 Picton earthquake's m_b (body wave magnitude), M_L (local magnitude), and M_S (surface-wave magnitude) values to M_W (moment magnitude) using equations recommended by Allen et al. (2018).

Magnitude Scale	Magnitude	Moment Magnitude Conversion Equation	Moment Magnitude
m_b	5.5	$1.2 \times m_b - 1.176$	5.424
M_L	5.5	$0.042 \times M_L^2 + 0.481 \times M_L + 1.395$	5.311
M_S	5.3	$0.075 \times M_S^2 + 3.357$	5.464

Two faults are implemented in Coulomb 3.4: the Burragorang fault and the Lapstone fault (Figure 3). The attitude of the Burragorang fault is inferred from the vertical nodal plane from the focal mechanisms in Figure 2, with a north-south strike and dipping 80 degrees east. The fault plane geometry is inferred from aftershock locations, with a horizontal length of 12 km and extends from 6 km to 30 km depth. Known faults in the area (e.g., Kurrajong Fault System; Figure 1b) have a similar attitude.

The Lapstone fault is a segment of the larger Lapstone Structural Complex, that runs subparallel to the Burragorang fault and strikes 16 km. Fergusson & Hatherly (2022) suggest a moderately west-dipping thrust fault at depth, though exact fault parameters are unknown. We infer a dip of 35 degrees west, down to 30 km depth, to approximately intersect the mainshock's location (Figure 3b), and approximates with the west dipping nodal plane of Figure 2c. We impose a depth limit from 1 to 30 km as the location of the deepest aftershock is at 31 km depth.

Four fault source and receiver models were created for ΔCFS analysis. Their slip direction is based on the nodal planes of published focal mechanisms (Figure 2 and Table 2). We assume reverse slip for the Lapstone and Burragorang fault based on either nodal planes in Figure 2b and c. Alternative strike-slip motion for the Burragorang fault is based on the vertical nodal plane of Figure 2d.The M_W of 5.4 is used to infer a rupture surface area of ~16 km^2 (Leonard, 2014). We subdivide the faults into a ~4 km by 4 km grid to represent the rupture surface area, and to visualise stress change through the fault. As such, there are two domains on any given source fault: the rupture area which encompasses a single grid square, and the receiver area which encompasses the rest of the fault (Figure 3). The receiver fault only has receiver area.

Table 2. Numbered fault models and its respective source and receiver faults with slip direction. The source fault hosts two domains: the rupture area (the blue square in Figure 3a) and receiver area (the white squares in Figure 3a).

Model Number	Source Fault (Slip Direction)	Receiver Fault (Slip Direction)
Model 1	Lapstone fault (reverse)	Burragorang fault (reverse)
Model 2	Lapstone fault (reverse)	Burragorang fault (strike-slip)
Model 3	Burragorang fault (reverse)	Lapstone fault (reverse)
Model 4	Burragorang fault (strike-slip)	Lapstone fault (reverse)

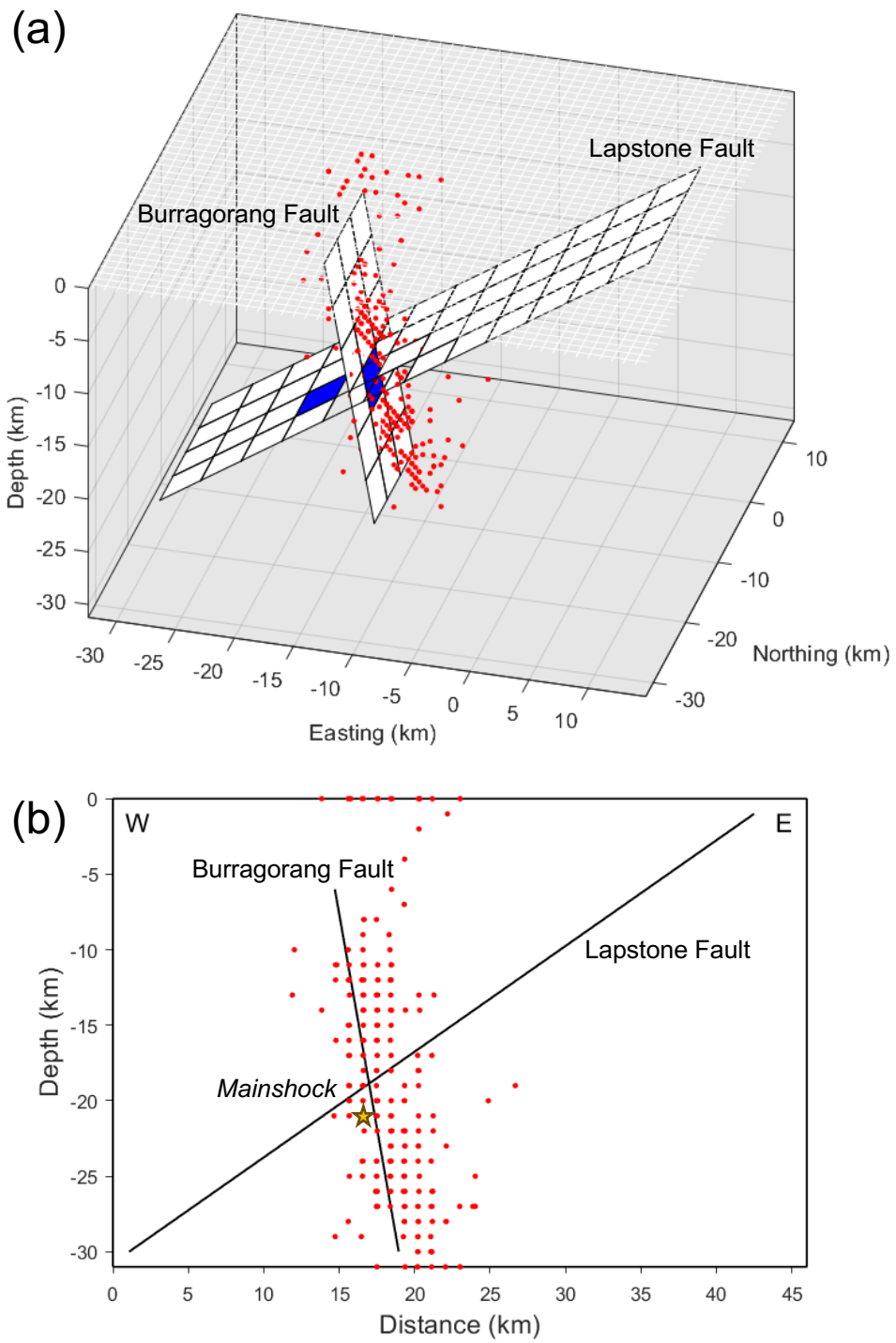

Figure 3. (a) 3D model; and (b) cross section of the Burragorang and Lapstone fault. The blue grid square in (a) represents the rupture area. The red points are aftershock locations. Earthquake data is sourced from Geoscience Australia (2023).

2.2 Focmec

We utilise the Focmec package by Snoke (2017) to create focal mechanisms based on polarities from the Fitch (1976) and Mills & Fitch (1977) station datasets (hereafter the original and updated station datasets, respectively) (Figure 2a). The purpose of using two datasets is to account for the uncertainty of the southwest quadrant take-off angles between 50 to 80 degrees, as shown in Figure 2a. Focmec performs a systematic search of all acceptable focal mechanisms based on user-determined polarity errors. We utilise the relative weighting method, which assigns an error value between 0 to 1 for any incorrectly placed polarity, depending on the distance from the nearest nodal plane (where an incorrect polarity closer to a nodal plane has a value closer to 0). Each focal mechanism is then assigned a weight equal to the sum of all polarities error value, where a lower weighted solution is more accurate.

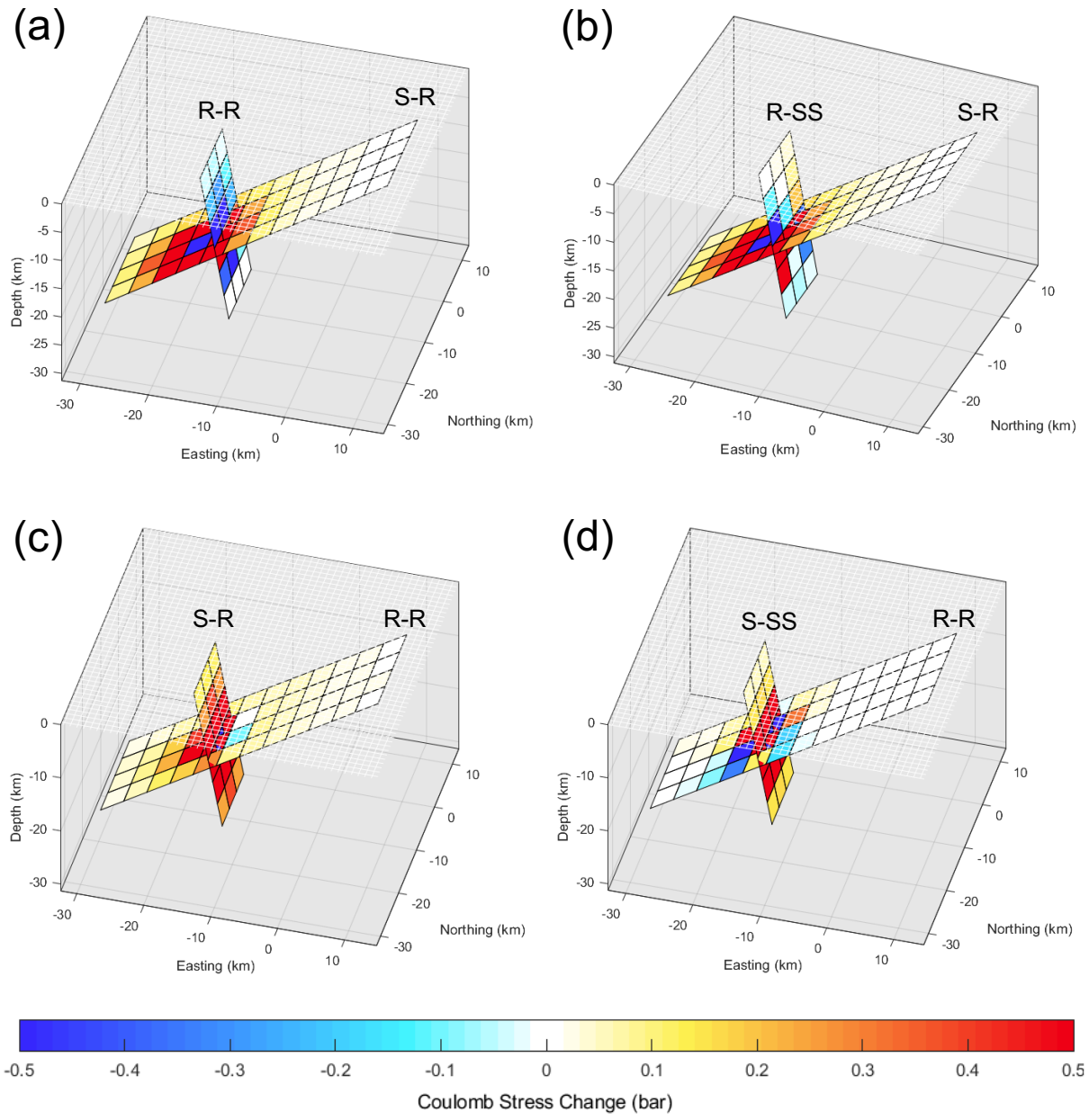

Figure 4. 3D models of coulomb stress change results of (a) model 1; (b) model 2; (c) model 3; and (d) model 4. The letter codes above each fault (e.g., S-R) refers to [fault type]-[slip direction] (e.g., Source-Reverse). For fault type, S = source fault and R = receiver fault. For slip direction, R = reverse and SS = strike-slip.

3 Results

3.1 Coulomb stress change

In Model 1, we observe an overall decrease in stress throughout the Burragorang fault, with a stress increase where the Lapstone fault intersects (Figure 4a). The lower portion of the Lapstone fault experiences a radial increase of stress from the rupture source. The stress largely dissipates past 12 km depth. Note that the rupture area will always experience a decrease in stress.

The Lapstone fault in Model 2 (Figure 4b) behaves identically to that in Model 1. The stress distribution in the Burragorang fault is more complex. In general, the highest stress change is focused on the intersection with the Lapstone fault and dissipates from the source.

Model 3 shows a stress increase throughout both faults (Figure 4c). In comparison to the Lapstone fault, the Burragorang fault experiences a higher stress increase radially from the rupture source.

The Burragorang fault in Model 4 shows a radial increase in stress from the rupture source (Figure 4d). The stress distribution on the Lapstone fault is complex, like that of the Burragorang fault in Model 2. Again, stress change is highest at the intersection of the two faults, with a checkered-like pattern in increase and decrease of stress.

3.2 Focmec

Similar strike-slip focal mechanisms were produced for ≤0.3 and ≤0.5 error solutions, for the original and updated datasets, respectively (Figure 5). For the original dataset, polarity errors up to 0.5 are no longer dominantly strike-slip and have some component of reverse motion (Figure 5a). The updated dataset shows a similar pattern, with polarity errors up to 1.0 incorporating some component of normal slip (Figure 5b).

The difference in error value between original and updated station datasets is likely due to the constraints imposed by southwest quadrant polarities. The lower take-off angle of the original dataset (~50 degrees) restricts possible solutions, while the higher take off angles of the updated dataset (~80 degrees) allows for more possible solutions in Focmec analysis.

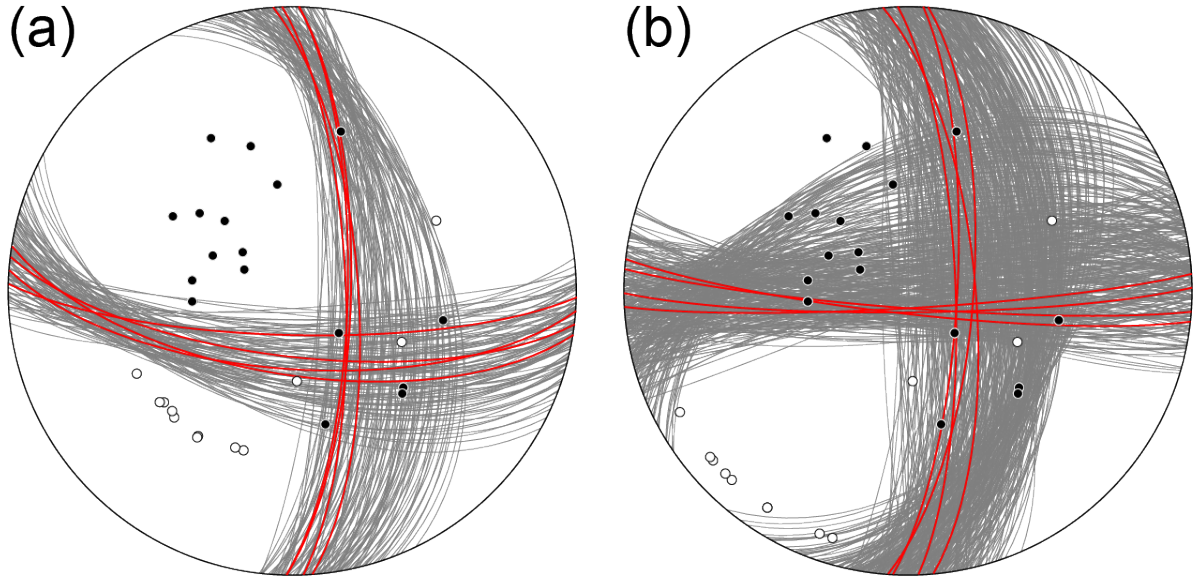

Figure 5. Focal mechanism solutions from the Focmec analysis. Compressional and dilatational polarities are represented by the solid and open circles, respectively. (a) Utilised the original station dataset. The red lines represent ≤0.3 error solutions. The grey lines represent ≤0.5 error solutions. (b) Utilised the updated dataset. The red lines represent ≤0.5 error solutions. The grey lines represent ≤1.0 error solutions.

4 Discussion

To account for the aftershock cluster, the best fault model for ΔCFS predicts an increase in stress along the Burragorang fault (excluding the rupture area), and a decrease or no change in stress along the Lapstone fault. Although Model 4 has some shortcomings (Figure 4d), it best aligns with these requirements. The Lapstone fault in Model 4 is sub-optimal due to some increase ΔCFS. The Lapstone fault in Models 1, 2, and 3 (Figure 4a, b, and c) are a poorer match to the expected stress change due to an overall stress increase.

Analysis of focal mechanisms provides additional support to the interpretation of the Burragorang fault as the source fault. Focmec analysis produced strike-slip focal mechanisms (with the lowest polarity uncertainty) from both the original and updated station datasets. The vertical nodal planes share the same characteristics as the Burragorang fault. This result supports the most recent strike-slip focal mechanism produced by Leonard et al. (2002). Additionally, reverse motion focal mechanisms similar to that shown in Figure 2b and c were not reproducible in our Focmec analysis. Hence, both ΔCFS and Focmec analysis indicates that the Burrangorang fault ruptured in a strike-slip fashion and was the likely source of the 1973 Picton earthquake.

The local geology and stress field are two other supporting lines of evidence for the Burragorang fault acting as the source fault. The Kurrajong Fault Complex to the north shares similar characteristics to the Burragorang fault, striking north-south and dipping steeply east. A lineament immediately south of the Burragorang fault also strikes north-south, though the dip and dip direction are unknown. New stress measurements from the updated 2016 Australian stress map database indicates a north-northeast maximum horizontal stress orientation for the Sydney Basin (Rajabi et al., 2017). This is consistent with strike-slip faulting on the Burragorang fault.

4.1 Limitations

In our models, the faults mapped are strictly planar. While a simple planar fault might be suitable for the Burragorang fault, a model of segmented trishear faulting has been proposed for the Lapstone fault (Fergusson & Hatherly, 2022). Furthermore, the two faults may intersect at depth, implying that some form of displacement at the intersection is warranted, but that was not included in our analysis. Whilst the upper depth of the Lapstone fault is informed by interpretations from Fergusson & Hatherly (2022), the depth of the base of the fault was simply chosen to match the depth of the Burragorang fault.

Other, more robust focal mechanisms software algorithms exist, such as HASH (Hardebeck & Shearer, 2002). However, they require data points that are typically lost or unavailable for older focal mechanism solutions. In our case, station names and locations, instrument accuracy, and the original data are missing or not assigned to a polarity. This information is key to understanding uncertainty of the measurements and station instrument reliability.

The location of the mainshock and aftershocks are likely to be poorly constrained given the sparsity of the seismic network, and are sensitive to crustal structure and velocity. For the Picton earthquake, velocity values of 6 and 3.6 km/s were assumed for P- and S-waves, respectively, for the sedimentary rocks of the Sydney Basin (Mills & Fitch, 1977). Mills & Fitch (1977) notes that these values are inconsistent with the refined take-off angles, which affected both the focal mechanism analysis and aftershock depth. Newer studies provide much more detailed models of velocity values (Kennett & Salmon, 2012; Chen et al., 2023). However, reanalysis is challenging without access to the original station dataset.

5 Conclusion

Using the 1973 Picton earthquake as a case study, we have ascertained a plausible hidden fault (the Burragorang fault) and proposed an improved focal mechanism. While the methodology presented in this paper has its limitations, it is can be easily and quickly applied to many old earthquakes and their aftershocks for the purpose of improving neotectonic fault mapping.

6 References

Allen, T. I. (2021). Simplified Fault Source Model Attributes. Canberra: Geoscience Australia.

Allen, T. I., Leonard, M., Ghasemi, H. & Gibson, G. (2018). The 2018 National Seismic Hazard Assessment for Australia: Earthquake Epicentre Catalogue. *In:* GEOSCIENCE AUSTRALIA (ed.). Canberra.

Australian Bureau of Statistics. (2022). *50 years of capital city population change* [Online]. ABS Website. Available: https://www.abs.gov.au/articles/50-years-capital-city-population-change [Accessed 6 July 2023].

Branagan, D. F. & Pedram, H. (1990). The Lapstone structural complex, New South Wales. Australian Journal of Earth Sciences, 37**,** 1, 23-36.

Chen, Y., Saygin, E., Kennett, B., Qashqai, M. T., Hauser, J., Lumley, D. & Sandiford, M. (2023). Next-generation seismic model of the Australian crust from synchronous and asynchronous ambient noise imaging. Nature Communications, 14**,** 1, 1192.

Colquhoun, G. P., Hughes, K. S., Deyssing, L., Ballard, J. C., Folkes, C. B., Phillips, G., Troedson, A. L. & Fitzherbert, J. A. (2022). New South Wales Seamless Geology dataset. *In:* GEOLOGICAL SURVEY OF NEW SOUTH WALES (ed.) 2.2 ed. Maitland.

Dayer, R. J. (1976). Some Structural Damage Caused by the 1973 Picton Earthquake. *Symposium on Seismicity and Earthquake Risk in Eastern Australia.* Canberra, Australia: Department of National Resources.

Denham, D. (1976). Effects of the 1973 Picton and Other Earthquakes in Eastern Australia. *Symposium on Seismicity and Earthquake Risk in Eastern Australia.* Canberra, Australia: Department of National Resources.

Fergusson, C. L., Bray, A. & Hatherly, P. (2011). Cenozoic Development of the Lapstone Structural Complex, Sydney Basin, New South Wales. Australian Journal of Earth Sciences, 58**,** 1, 49-59.

Fergusson, C. L. & Hatherly, P. J. (2022). Segmentation and fault–monocline relationships in the Lapstone Structural Complex, Sydney Basin, New South Wales. Australian Journal of Earth Sciences**,** 1-18.

Fitch, T. J. (1976). The Picton Earthquake of 9 March 1973: A Seismic View of the Source. *Symposium on Seismicity and Earthquake Risk in Eastern Australia.* Canberra, Australia: Department of National Resources.

Gallant, J., Wilson, N., Dowling, T., Read, A., Inskeep, C. (2011). SRTM-derived 1 Second Digital Elevation Models. *In:* GEOSCIENCE AUSTRALIA (ed.) 1.0 ed. Canberra.

Geoscience Australia. (2023). *Earthquakes@GA* [Online]. Available: https://earthquakes.ga.gov.au/ [Accessed 1 August 2023].

Hardebeck, J. L. & Shearer, P. M. (2002). A New Method for Determining First-Motion Focal Mechanisms. Bulletin of the Seismological Society of America, 92**,** 6, 2264-2276.

Kennett, B. L. N. & Salmon, M. (2012). AuSREM: Australian Seismological Reference Model. Australian Journal of Earth Sciences, 59**,** 8, 1091-1103.

Kilb, D., Gomberg, J. & Bodin, P. (2002). Aftershock triggering by complete Coulomb stress changes. Journal of Geophysical Research: Solid Earth, 107**,** B4, ESE 2-1-ESE 2-14.

King, G. C. P., Stein, R. S. & Lin, J. (1994). Static stress changes and the triggering of earthquakes. Bulletin of the Seismological Society of America, 84**,** 3, 935-953.

Leonard, M. (2014). Self-Consistent Earthquake Fault-Scaling Relations: Update and Extension to Stable Continental Strike-Slip Faults. Bulletin of the Seismological Society of America, 104**,** 6, 2953-2965.

Leonard, M., Ripper, I. D. & Yue, L. (2002). Australian earthquake fault plane solutions. Canberra: Geoscience Australia.

Lin, J. & Stein, R. S. (2004). Stress triggering in thrust and subduction earthquakes and stress interaction between the southern San Andreas and nearby thrust and strike-slip faults. Journal of Geophysical Research: Solid Earth, 109**,** B2.

Mills, J. M. & Fitch, T. J. (1977). Thrust faulting and crust—upper mantle structure in East Australia. Geophysical Journal International, 48**,** 3, 351-384.

Rajabi, M., Tingay, M., Heidbach, O., Hillis, R. & Reynolds, S. (2017). The present-day stress field of Australia. Earth-Science Reviews, 168**,** 165-189.

Snoke, J. A. (2017). FOCMEC: Focal mechanism determinations. 1-31.

Toda, S., Stein, R. S., Richards-Dinger, K. & Bozkurt, S. B. (2005). Forecasting the evolution of seismicity in southern California: Animations built on earthquake stress transfer. Journal of Geophysical Research: Solid Earth, 110**,** B5.

Toda, S., Stein, R. S., Sevilgen, V. & Lin, J. (2011). Coulomb, 3.3 Graphic-rich deformation and stress-change software for earthquake, tectonic, and volcano research and teaching-user guide. *In:* SURVEY, U. S. G. (ed.). Reston, Virginia.

Van der beek, P., Pulford, A. & Braun, J. (2001). Cenozoic Landscape Development in the Blue Mountains (SE Australia): Lithological and Tectonic Controls on Rifted Margin Morphology. The Journal of Geology, 109**,** 1, 35-56.

Ziv, A. & Rubin, A. M. (2000). Static stress transfer and earthquake triggering: No lower threshold in sight? Journal of Geophysical Research: Solid Earth, 105**,** B6, 13631-13642.